Mon. Not. R. Astron. Soc. **385,** 1129–1142 (2008) doi:10.1111/j.1365-2966.2008.12936.x

Mapping of molecular gas inflow towards the Seyfert nucleus of NGC 4051 using Gemini NIFS

Rogemar A. Riffel,[1]★ Thaisa Storchi-Bergmann,[1] Cláudia Winge,[2] Peter J. McGregor,[3] Tracy Beck[4] and Henrique Schmitt[5,6]

[1]*Universidade Federal do Rio Grande do Sul, IF, CP 15051, Porto Alegre 91501-970, RS, Brazil*
[2]*Gemini Observatory, c/o AURA Inc., Casilla 603, La Serena, Chile*
[3]*Research School of Astronomy and Astrophysics, Australian National University, Cotter Road, Weston Creek, ACT 2611, Australia*
[4]*Gemini Observatory, Northern Operations, Hilo, HI, USA*
[5]*Remote Sensing Division, Naval Research Laboratory, 4555 Overlook Avenue, SW, Washington, DC 20375, USA*
[6]*Interferometric Inc., 13454 Sunrise Valley, Suite 240, Herndon, VA 20171, USA*

Accepted 2008 January 8. Received 2008 January 8; in original form 2007 December 3

ABSTRACT

We present 2D stellar and gaseous kinematics of the inner $\sim 130 \times 180$ pc^2 of the Narrow-Line Seyfert 1 galaxy NGC 4051 at a sampling of 4.5 pc, from near-infrared *K*-band spectroscopic observations obtained with the Gemini's Near-infrared Integral Field Spectrograph (NIFS) operating with the ALTAIR adaptive optics module. We have used the CO absorption band heads around 2.3 μm to obtain the stellar kinematics which show the turnover of the rotation curve at only ≈55 pc from the nucleus, revealing a highly concentrated gravitational potential. The stellar velocity dispersion of the bulge is ≈60 km s^{-1} – implying on a nuclear black hole mass of $\approx 10^6$ M$_\odot$ – within which patches of lower velocity dispersion suggest the presence of regions of more recent star formation. From measurements of the emission-line profiles we have constructed 2D maps for the flux distributions, line ratios, radial velocities and gas velocity dispersions for the H_2, H II and [Ca VIII] emitting gas. Each emission-line samples a distinct kinematics. The Brγ emission-line shows no rotation as well as no blueshifts or redshifts in excess of 30 km s^{-1}, and is thus not restricted to the galaxy plane. The [Ca VIII] coronal region is compact but resolved, extending over the inner 75 pc. It shows the highest blueshifts – of up to -250 km s^{-1}, and the highest velocity dispersions, interpreted as due to outflows from the active nucleus, supporting an origin close to the nucleus. Subtraction of the stellar velocity field from the gaseous velocity field has allowed us to isolate non-circular motions observed in the H_2 emitting gas. The most conspicuous kinematic structures are two nuclear spiral arms – one observed in blueshift in the far side of the galaxy (to the north-east), and the other observed in redshift in the near side of the galaxy (to the south-west). We interpret these structures as inflows towards the nucleus, a result similar to those of previous studies in which we have found streaming motions along nuclear spirals in ionized gas using optical Integral Filed Unit (IFU) observations. We have calculated the mass inflow rate along the nuclear spiral arms, obtaining $\dot{M}_{H_2} \approx 4 \times 10^{-5}$ M$_\odot$ yr^{-1}, a value ∼100 times smaller than the accretion rate necessary to power the active nucleus. This can be understood as due to the fact that we are only seeing the hot 'skin' (the H_2 emitting gas) of the total mass inflow rate, which is probably dominated by cold molecular gas. From the H_2 emission-line ratios we conclude

★E-mail: rogemar@ufrgs.br

that X-ray heating can account for the observed emission, but the H_2 λ2.1218 μm/Br γ line ratio suggests some contribution from shocks in localized regions close to the compact radio jet.

Key words: galaxies: individual: NGC 4051 – galaxies: kinematics – galaxies: Seyfert – infrared: galaxies.

1 INTRODUCTION

The presence of supermassive black holes (SMBHs) at the centres of all galaxies which have stellar bulges is nowadays widely accepted by the astronomy community (Ferrarese & Merritt 2000; Gebhardt et al. 2000). According to this scenario the energy emitted by an active galactic nucleus (AGN) is due to the accretion of material on to the SMBH and implies the presence of a gas reservoir close to the AGN. Simões Lopes et al. (2007) using archival *Hubble Space Telescope* (*HST*) optical images for a large sample of early-type galaxies with and without AGNs, found that all AGN hosts have circumnuclear gas and dust, while this is observed in only 26 per cent of a pair-matched sample of inactive galaxies. A gas reservoir close to the AGN is also supported by the presence of recent star formation in the circumnuclear region of active galaxies (Schmitt, Storchi-Bergmann & Cid Fernandes 1999; Boisson et al. 2000; Storchi-Bergmann et al. 2000; Cid Fernandes et al. 2001, 2005; Storchi-Bergmann et al. 2005). However, the strongest signatures that feeding to the SMBH is occurring include the observation of streaming motions in ionized gas along nuclear spirals towards the nucleus of nearby active galaxies using 2D optical spectroscopy (Fathi et al. 2006; Storchi-Bergmann et al. 2007).

Streaming motions as feeding signatures to the nuclear region have been previously observed in radio wavelengths. Adler & Westpfahl (1996), for example, have found streaming motions towards the centre along the spiral arms of M 81 in H I, while Mundell & Shone (1999) have found similar streaming motions towards the nucleus along the weak bar of NGC4151. Closer to the centre, most of the gas is in the molecular phase, and CO observations have been used to map the gas kinematics and inflows (e.g. García-Burillo et al. 2003; Krips et al. 2005; Boone et al. 2007).

Molecular hydrogen emission lines are also relatively strong in the near-infrared (near-IR) *K*-band spectra of active galaxies, and previous studies suggest that its distribution and kinematics is distinct from that observed in the other emission lines, which are usually dominated by outflows (e.g. Crenshaw & Kraemer 2000; Das et al. 2005). In the Seyfert galaxies NGC 2110 and Circinus, for example, Storchi-Bergmann et al. (1999) have found broader emission-line profiles for [Fe II] and Paβ than for the H_2λ2.1218 μm emission line in a study using near-IR long-slit observations, suggesting a stronger influence of nuclear outflows on the former emission lines and a different origin for the H_2 emitting gas, consistent with the colder kinematics of the galaxy disc. More recently, using 2D near-IR spectroscopy of the Seyfert galaxy ESO 428−G14, we (Riffel et al. 2006b) have found that the H_2 emission distribution was mostly restricted to the plane of the galaxy and was less affected by the AGN outflow than the [Fe II] and Paβ emission lines.

In this paper we use adaptive optics Integral Filed Unit (IFU) spectroscopic data obtained with the Gemini's Near-infrared Integral Field Spectrograph (NIFS; McGregor et al. 2003), in the near-IR *K* band at a sampling of 0.1 × 0.1 arcsec^2, to investigate the stellar and gaseous kinematics of the inner ∼ 3 × 4 arcsec^2 of the nearby active galaxy NGC 4051. The stellar kinematics will be used to constrain the galaxy potential and mass of the SMBH, but our main goal is to look for signatures of feeding mechanisms at parsec scales through the H_2 kinematics.

NGC 4051 is a SABbc galaxy at a distance of only ∼9.3 Mpc (Barbosa et al. 2006), such that 1.0 arcsec corresponds to 45 pc at the galaxy. It harbours one of the closest AGN, classified as a Narrow-Line Seyfert 1 (NLS1). We have selected NGC 4051 for this study partially on the basis of the recent work of Barbosa et al. (2006), who obtained 2D stellar kinematics using the IFU of the Gemini Multi-Object Spectrograph (GMOS) to observe the stellar absorption lines of the calcium triplet around 8500 Å. These authors have shown that the turnover of the stellar rotation curve occurs at only $R \sim 50$ pc from the nucleus, indicating that the stellar motions are dominated by a highly concentrated gravitational potential. As NIFS with the ALTAIR adaptive optics module provides a much better image sampling and resolution than the GMOS-IFU, we decided to further investigate the kinematics of the nuclear region of NGC 4051 in order to better constrain the gravitational potential and the mass of the SMBH. In addition, this galaxy shows strong H_2 emission (Riffel, Rodríguez-Ardila & Pastoriza 2006a), making it a good candidate for a study of its kinematics.

Previous studies of NGC 4051 include *HST* narrow-band [O III] images which show an unresolved nuclear source and faint extended emission (by 1.2 arcsec) along the position angle PA = 100° (Schmitt & Kinney 1996), the approximate direction of the alignment of two radio components at 6 cm separated by 0.4 arcsec (Ulvestad & Wilson 1984). Veilleux (1991) reported that the profiles of optical forbidden emission lines present blue wings reaching velocities of up to 800 km s^{-1}, and proposed a model for the narrow-line region (hereafter NLR) with outflows and obscuring dust. Evidence for outflows have also been observed by Christopoulou et al. (1997) for the [O III] emission to 1.5 arcsec north-east of the nucleus. Nagao, Taniguchi & Murayama (2000) using the [Fe X]λ6374 emission line report a high ionization region extending to 3.0 arcsec south-east of the nucleus. Lawrence et al. (1985) found a X-ray variability on time-scales of the order of 1 h and Salvati et al. (1993) reported flux changes by a factor of 2 in 6 months observed at 2.2 μm and suggest that emission by dust reprocessing of the ultraviolet (UV) radiation from the nucleus is an acceptable explanation. Ponti et al. (2006) modelled the nuclear emission by two power-law components, one due to the AGN and other due to reflection by the accretion disc.

This paper is organized as follows. In Section 2 we describe the observations and data reduction. In Section 3 we present the results for the stellar kinematics. In Section 4 we present the emission-line flux distributions and in Section 5 we present the results for the gas kinematics. In Section 6 we discuss the results and in Section 7 we present the conclusions of this work.

2 OBSERVATIONS AND DATA REDUCTION

The IFU spectroscopic data were obtained with NIFS operating with the ALTAIR adaptive optics module on the 8-m Gemini North telescope in 2006 January under the instrument science verification programme GN-2006A-SV-123. The IFU has a square field of view of $\approx 3.0 \times 3.0$ arcsec^2, divided into 29 slices with an angular sampling of 0.1×0.04 arcsec^2. The observing procedures followed the standard object–sky–sky–object dither sequence, with off-source sky positions since the target is extended, and individual exposure times of 750 s centred at $\lambda = 2.2499$ μm. Two sets of observations, each with three individual exposures, were obtained at different spatial positions; the first one centred at the position 0.4 arcsec from the nucleus along PA $= -74^\circ$ and the second at a position offset 0.5 arcsec along PA $= 106^\circ$. The longest extent covered by the IFU observations was oriented along PA $= 106^\circ$, which corresponds to the orientation of the line of nodes derived by modelling of the stellar velocity field with a rotating disc (Barbosa et al. 2006). We have used the K_G5605 grating and the filter HK_G0603, which resulted in an arc lamp line full width at half-maximum (FWHM) of 3.2 Å.

The data reduction was accomplished using tasks contained in the NIFS package which is part of GEMINI IRAF package as well as generic IRAF tasks. The reduction procedure included trimming of the images, flat-fielding, sky subtraction, wavelength and s-distortion calibrations. We have also removed the telluric bands and flux calibrated the frames by interpolating a blackbody function to the spectrum of the telluric standard star. The final IFU data cube contains 1160 spectra, each spectrum corresponding to an angular coverage of 0.1×0.1 arcsec^2, which translates into 4.5×4.5 pc^2 at the galaxy and covering the spectral region from 1.991 to 2.425 μm. The total observed field of view 2.9×4.0 arcsec^2 (obtained by mosaicking the two set of observations) thus corresponds to a region of projected dimensions 130×180 pc at the galaxy.

In the top left-hand panel of Fig. 1 we present a large-scale *K*-band image from Knapen et al. (2003) obtained at the William Herschel Telescope (WHT). The central rectangle shows the IFU field of view. The large-scale image was rotated to the same orientation of the IFU observations. In the top right-hand panel we present an image obtained from the NIFS data cube for the 2.12 μm continuum emission, obtained by interpolation of the continuum under the H_2 λ2.1218 μm emission line. In the bottom panels we present three characteristic IFU spectra: the nuclear spectrum (position N in the continuum map), a spectrum from a location at 1.2 arcsec east of the nucleus (position A) and another from 0.75 arcsec west of the nucleus (position B). Both spectra correspond to an aperture of 0.3×0.3 arcsec^2. The emission lines are identified in the nuclear spectrum: the H_2 lines at $\lambda = 2.0338$, 2.1218 and 2.2235 μm, the H II Brγ at 2.1661 μm and the [Ca VIII] coronal emission line

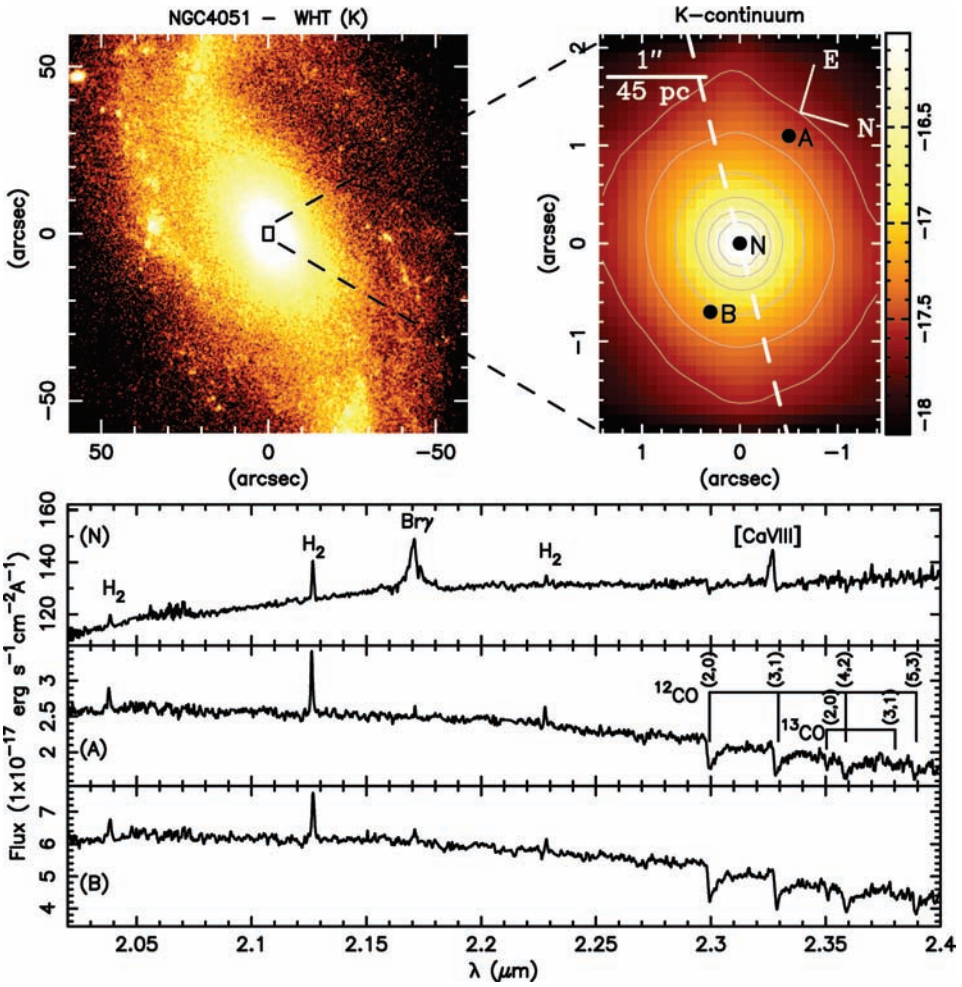

Figure 1. Top left-hand panel: WHT *K*-band large-scale image of NGC 4051 from Knapen et al. (2003). The image has been rotated to the same orientation of the NIFS observations. The box represents the IFU field of view. Top right-hand panel: 2.12-μm continuum map from IFU spectroscopy. Bottom: spectra at the positions N, A and B marked at the top right-hand panel with the emission lines and CO absorption band heads identified.

at 2.3211 μm. The ^{12}CO and ^{13}CO absorption band heads used to obtain the stellar kinematics are identified in the spectrum from position A.

3 LINE-OF-SIGHT VELOCITY DISTRIBUTION

In order to obtain the line-of-sight velocity distribution (LOSVD) we have used the penalized pixel fitting (PPXF) method of Cappellari & Emsellem (2004) to fit the stellar absorptions present in the *K*-band spectra. The algorithm finds the best fit to a galaxy spectrum by convolving a template stellar spectrum with the corresponding LOSVD. This procedure gives as output the radial velocity, velocity dispersion and higher order Gauss–Hermite moments. The PPXF method allows the use of several template stellar spectra and to vary the weights of the contribution of the different templates to obtain the best fit, minimizing the template mismatch problem. However, the use of PPXF requires templates which match closely the galaxy spectrum. Emsellem et al. (2004) present an extensive discussion about the use of the PPXF method and the templates mismatch problem and Silge & Gebhardt (2003) present a discussion about template mismatch for kinematic fitting using the CO absorption band heads in the near-IR.

A high signal-to-noise ratio (S/N) is required for reliable stellar kinematic measurements using the PPXF method. In previous works the data are usually binned to give S/N between 40 and 60 over the whole field of view. In our data, ratios smaller than these are observed only very close to the borders of the field (S/N $\approx$ 35 measured blueward of the first CO band head). Our typical S/N values are 80 with maximum values reaching 120 close to the nucleus, thus allowing reliable kinematic measurements without spatial binning of the data.

3.1 The stellar templates

In this study we have selected as template spectra, those of the spectroscopic library of late spectral type stars observed with the Gemini Near-Infrared Spectrograph (GNIRS) IFU using the grating 111 lines mm^{-1} in the *K* band (Winge, Riffel & Storchi-Bergmann 2007). This library is composed of spectra of 29 objects, which include dwarf, giant and subgiant stars with spectral types from F7 III to M3 III, observed in the spectral range from 2.24 to 2.42 μm. Of these, 23 stars were also observed on a second setting extending the wavelength coverage down to 2.15 μm. The spectra of the templates have S/N values larger than 50 blueward of the CO 2–0 first-overtone band head. Detailed discussion about this library is presented by Winge et al. (2007). The spectral resolution of the stellar spectra is 3.3 Å – very close to the spectral resolution of the NIFS data, thus the library can be used to fit the stellar kinematics without any resolution correction. We have verified this in some tests using available NIFS spectra of a few stars. We opted to use the GNIRS library because there are too few available template spectra with NIFS. We have chosen 16 stars from the library which better match the stellar features of NGC 4051.

In order to investigate the influence of the stellar templates on the velocity dispersions obtained we have fitted the stellar kinematics using individual stars as templates. We observed that the large-scale structures in σ maps are similar for all stars, but the mean σ values vary significantly – higher equivalent widths in the templates result in lower σ values for the galaxy. This result evidences the importance of using a large library of stellar templates in order to obtain reliable velocity dispersion measurements.

3.2 The effect of the [Ca VIII] coronal line

The nuclear spectrum of NGC 4051 (Fig. 1) shows the coronal emission line of [Ca VIII] at 2.3211 μm. Davies et al. (2006) have shown that this line affects the kinematic measurements obtained from the CO band heads. In order to investigate the influence of this line in our measurements, we have chosen two spectral regions to fit the stellar kinematics: the first one (2.258–2.372 μm) includes the [Ca VIII] line and the second (2.258–2.314 μm and 2.346–2.372 μm) excludes this line (together with the 'contaminated' CO band head). We observed that the radial velocities and velocity dispersions derived using the first spectral range are higher in the nuclear region, where the [Ca VIII] emission line is present, than those obtained by using the second spectral region. We thus decided to exclude the contaminated ^{12}CO 3–1 band head from the stellar kinematics fitting in the region where the [Ca VIII] emission line is present (the central 0.8 arcsec radius). In regions away from the nucleus we used the first spectral range which includes the ^{12}CO 3–1 band head.

3.3 The stellar kinematics

In Fig. 2 we show the fits of the stellar templates to the galaxy spectra with the program PPXF for four different positions: the nucleus; 1.2 arcsec south-east and 1.2 arcsec north-west of the nucleus, where we observe the turnovers of the rotation curve and a location at 1.5 arcsec east of the nucleus, almost at the border of the NIFS field. We observe that the stellar templates fit very well the galaxy spectra at most positions, including regions near the border of the IFU field, where the S/N is smaller. The results for the nucleus should nevertheless be considered with caution, as the fitting may have been affected by dust emission and emission lines present in the galaxy spectrum but absent in the stellar templates.

In Fig. 3 we present the resulting stellar kinematics. The black regions in this figure are masker regions where the S/N in the spectra was too low to provide a reliable fit. In the top left-hand panel we show the stellar velocity field, which shows a velocity range from ≈ -40 to $\approx$40 km s^{-1} with the turnover occurring at $\approx$55 pc from the nucleus in good agreement with the velocity field obtained by Barbosa et al. (2006) from optical IFU data. The mean uncertainties in the velocities are $\approx$ 10 km s^{-1}. The turnover and amplitude of the rotation curve can be more easily observed in the 1D cut of the stellar velocity field shown in Fig. 4. The 1D rotation curve was obtained by the average of the velocities within a pseudo-slit with 1 arcsec width oriented along the major axis of the galaxy.

The stellar velocity dispersion map is shown in the top right-hand panel of Fig. 3. The σ map presents values ranging from $\approx$35 to $\approx$90 km s^{-1}, with mean uncertainties of $\approx$8 km s^{-1}. The bottom panels show the higher order Gauss–Hermite moments h_3 (left-hand side) and h_4 (right-hand side). These moments measure deviations of the line profile from a Gaussian: the parameter h_3 measures asymmetric deviations and the h_4 measure symmetric deviations (van der Marel & Franx 1993). The values h_3 and h_4 vary from -0.15 to 0.15 with mean uncertainties of 0.03. The highest values of h_3 are observed to south-east of the nucleus and the lowest values to north-west of the nucleus. The h_4 values are nearly zero over most of the IFU field.

3.4 Kinematic modelling

Since the stellar velocity field is dominated by rotation, it was fitted with a velocity model produced by a Plummer potential in order to obtain the systemic velocity, orientation of the line of nodes,

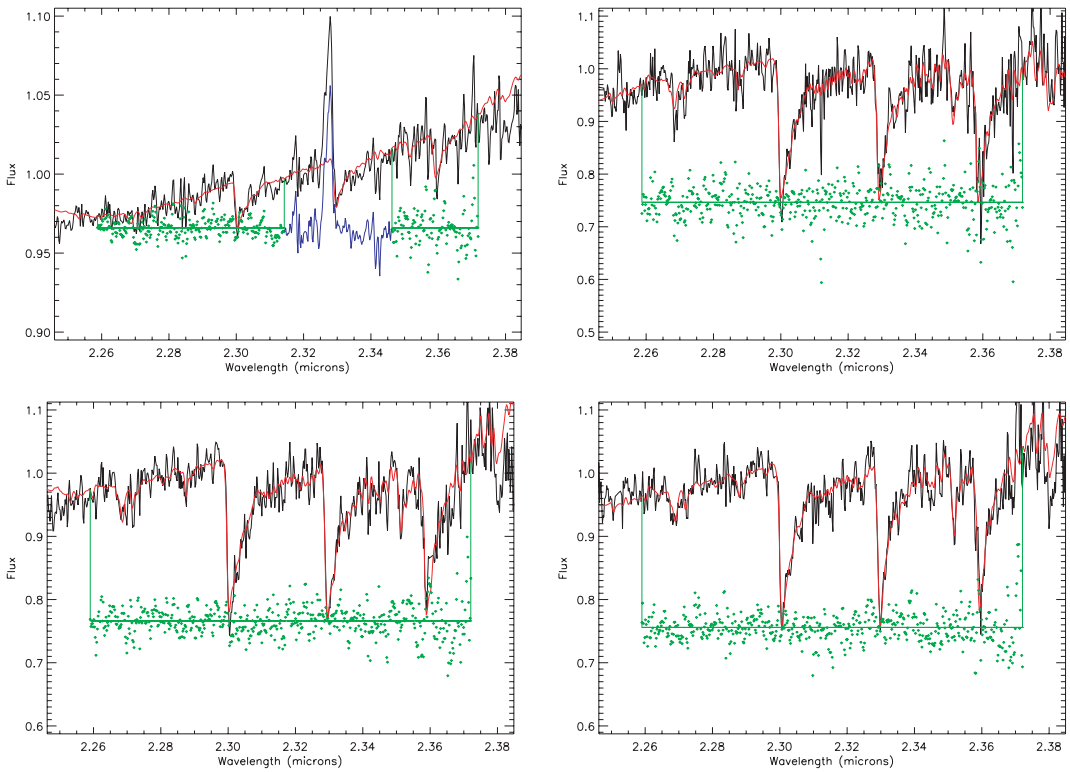

Figure 2. Sample fits of the stellar kinematics of the nuclear region of NGC 4051 using PPXF. Top left-hand panel: fit of the nuclear spectrum; top right-hand panel: fit of the spectrum at 1.5 arcsec east of the nucleus; bottom left-hand panel: fit of the spectrum at the location corresponding to the blue turnover of the rotation curve at 1.2 arcsec south-east of the nucleus; bottom right-hand panel: fit of the spectrum at the position of the red turnover of the rotation curve at 1.2 arcsec north-west of the nucleus. The observed spectra are shown in black, the fits in red, the residuals in green, while in blue we show the spectral range not included in the fit of the central region.

bulge mass and the position of the kinematical centre. The Plummer potential is given by

$$\Phi = -\frac{GM}{\sqrt{r^2 + a^2}}, \tag{1}$$

where a is a scalelength, r is the radial distance in the plane of the galaxy, M is the mass inside r and G is the Newton's gravitational constant. Defining the coordinates of the kinematical centre of the system as (X_0, Y_0), the observed radial velocity at position (R, Ψ), where R is the projected radial distance from the nucleus in the plane of the sky and Ψ is the corresponding PA, is given by (Barbosa et al. 2006)

$$V_r = V_s + \sqrt{\frac{R^2 GM}{(R^2 + A^2)^{3/2}}} \times \frac{\sin(i)\cos(\Psi - \Psi_0)}{\left[\cos^2(\Psi - \Psi_0) + \sin^2(\Psi - \Psi_0)/\cos^2(i)\right]^{3/4}}, \tag{2}$$

where V_s is the systemic velocity, i is the inclination of the disc ($i = 0$ for face on disc) and Ψ_0 is the PA of the line of nodes. The relations between r and R, and between a and A are $r = \alpha R$ and $a = \alpha A$, where $\alpha = \sqrt{\cos^2(\Psi - \Psi_0) + \sin^2(\Psi - \Psi_0)/\cos(i)}$. The equation above contains six free parameters, including the kinematical centre, which can be determined by fitting the model to the observations. This was done using a Levenberg–Marquardt least-squares fitting algorithm, in which initial guesses are given for the free parameters. As the inclination of the disc is tightly coupled with M as $V_r^2 \propto M \sin(i)$, it cannot be left as a free parameter. We have adopted the value of i = 414, an estimate obtained from $\cos(i) = b/a$, where b and a are the semiminor and semimajor axis of the large-scale disc as quoted in the NASA/IPAC Extragalactic Database (NED) for this galaxy.

The parameters derived from the fit are the systemic velocity corrected by the observatory motion relative to the local standard of rest, $V_s = 716 \pm 11\,\mathrm{km\,s^{-1}}$, $\Psi_0 = 120^\circ \pm 1^\circ$, $M = 7.7 \pm 0.6 \times 10^7\,\mathrm{M_\odot}$ and $A = 39.7 \pm 2.7\,\mathrm{pc}$. The derived kinematical centre is very close to the peak of the continuum emission, with $X_0 = 4.9 \pm 1.4\,\mathrm{pc}$ and $Y_0 = 3.1 \pm 1.2\,\mathrm{pc}$, where X_0 and Y_0 are measured in relation to the location corresponding to the peak of the continuum.

In Fig. 5 we present the derived rotation model in the left-hand panel and the residuals of the stellar velocity field (observed minus modelled) in the right-hand panel. We conclude that the stellar velocity field is well described by the Plummer potential – the residuals are close to zero over most of the IFU field. The highest residuals ($\sim$20 km s^{-1}) are observed within $\sim$0.3 arcsec from the nucleus, where the stellar kinematics fitting may have been affected by emission by dust and emission lines.

4 EMISSION-LINE FLUX DISTRIBUTIONS

We have fitted Gaussians to the observed emission-line profiles in order to obtain the integrated flux, radial velocity (from the central wavelength of the line) and velocity dispersion (from the width of the line). The corresponding flux maps are shown in Fig. 6. The H_2 $\lambda =$ 2.0338, 2.1218 and 2.2235 μm flux distributions are presented in the top left-hand, middle and right-hand panels, respectively, with mean uncertainties of 16 per cent, for the first one, 5 per cent for the second one and 9 per cent for the third one. Black regions identify locations

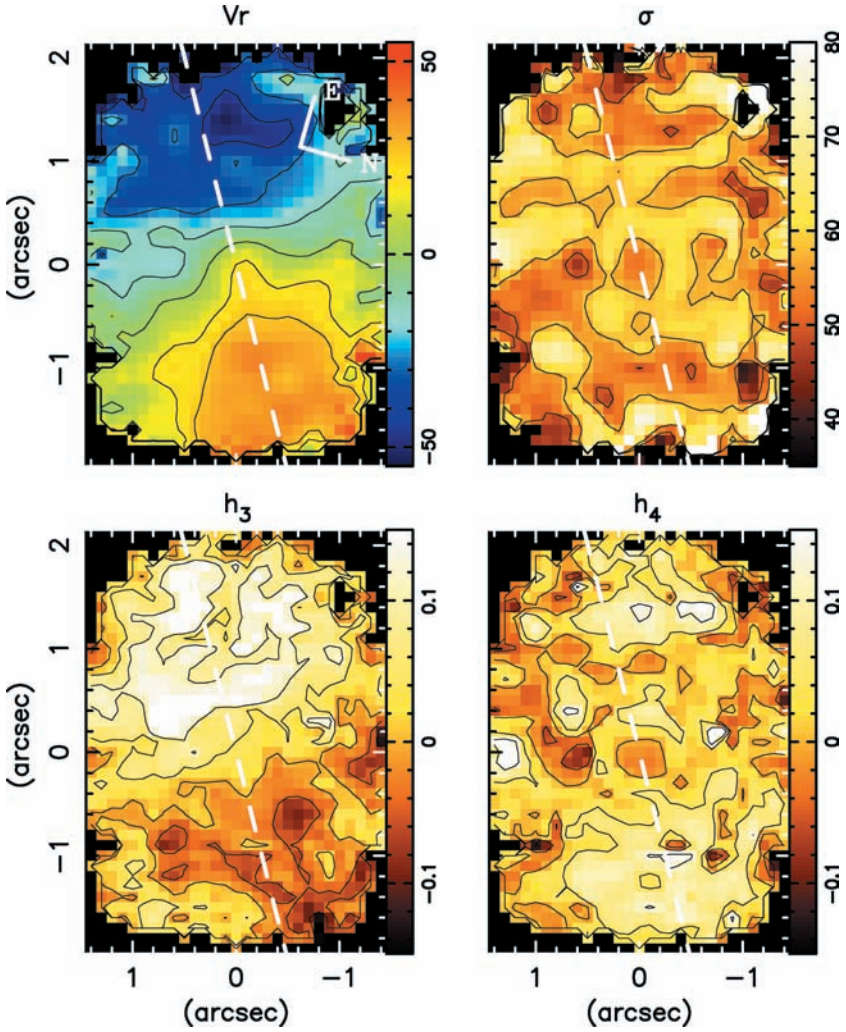

Figure 3. Stellar kinematic maps obtained from the PPXF fit. Top: radial velocity (left-hand side) and velocity dispersion (right-hand side) maps. Bottom: h_3 and h_4 Gauss–Hermite moments. The mean uncertainties are 10 km s^{-1} for radial velocity, 8 km s^{-1} for σ and 0.03 for h_3 and h_4. The dashed lines show the position of the line of nodes.

where the line fitting failed due to low S/N values. The molecular hydrogen emission is extended over most of the observed field. The highest flux values are observed at the nucleus, defined as the location of the peak of the continuum emission. The H_2 distribution is extended towards the north-east, between the direction of the radio axis (adopted as the one which connects the two radio peaks) and the line of nodes. The H_2 flux distribution shows also a good agreement with the [O III] narrow-band image from Schmitt & Kinney (1996), whose contours are overplotted in green on the top right-hand panel of Fig. 6.

The flux map in the Brγ narrow component is shown in the bottom left-hand panel of Fig. 6. In the central region ($r < 25$ pc) we have fitted two Gaussian components in order to separate the narrow and broad emission-line contributions, while in regions further away from the nucleus a single Gaussian was enough for the fit. The S/N in the top $\sim$1 arcsec of the observed field was not high enough to allow the measurement of this line and this is why the region appears black in Fig. 6. The mean flux uncertainty for Brγ is 24 per cent. The Brγ flux distribution has the highest flux values at the nucleus and is approximately symmetric around the nucleus, not showing any elongation as observed in the H_2 emitting gas.

The flux map of the [Ca VIII] λ2.3211 μm coronal emission line is presented in the bottom middle panel, where the mean flux uncertainties are 15 per cent. The [Ca VIII] emission peaks at the nucleus and is resolved, extending up to 0.8 arcsec from the nucleus, which corresponds to a projected distance of 36 pc at the galaxy.

The line ratio H_2 λ2.1218 μm/Brγ (only narrow component for Brγ) can be used as a diagnostic for the excitation mechanism of the molecular hydrogen emission lines (e.g. Riffel et al. 2006b), with higher H_2/Brγ ratios being interpreted as a larger contribution from shocks or X-ray to the H_2 excitation. We present this line ratio map in the bottom right-hand panel of Fig. 6. The lowest values are H_2 λ2.1218 μm/Brγ $\approx$1 observed at the nucleus and to the north. The highest values reach H_2 λ2.1218 μm/Brγ $\approx$ 8 and are observed predominantly in two regions, one approximately at 1.0 arcsec west of the nucleus and another at 0.8 arcsec east of the nucleus. We note that these two regions are close to the tips of the compact 3.6-cm radio structure (black contours in the top middle panel). Nevertheless, such a direct interpretation of this map should be considered with caution, as the flux distributions and kinematics (see next section) are obviously different for the H_2 and Brγ emission lines, implying that may originate in different regions of the galaxy.

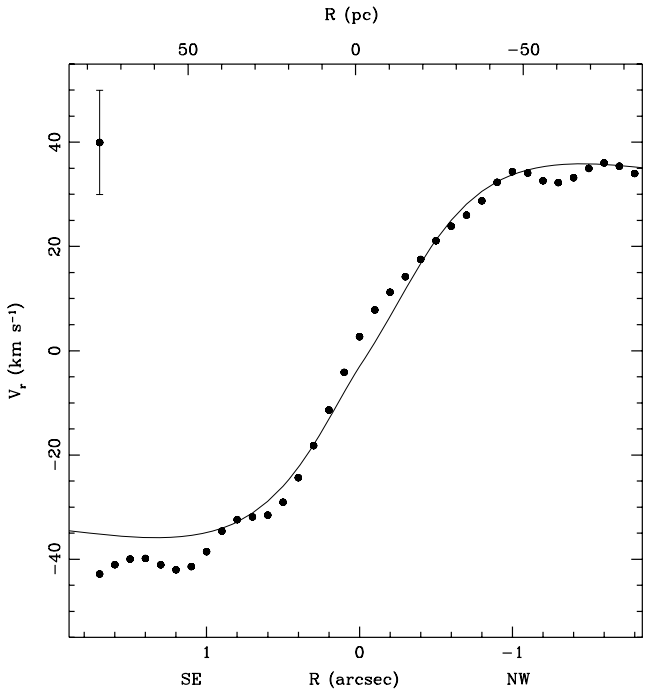

Figure 4. 1D stellar rotation curve for a pseudo-slit oriented along the major axis of the galaxy. The points are the observed radial velocities and the full line is the modelled velocities.

5 GAS KINEMATICS

In the left-hand panels of Fig. 7 we present the radial velocity field obtained from the central wavelengths of the H_2 λ2.1218 μm and Brγ emission lines, with mean uncertainties of 4 and 9 km s^{-1}, respectively. We chose the H_2 λ2.1218 μm line to represent the H_2 velocity as it is stronger and thus present smaller uncertainties in the measurements than the other H_2 emission lines. The systemic velocity of the galaxy, derived from the stellar kinematics modelling, has been subtracted from all the emission-line velocity plots.

The H_2 velocity field shows a 'rotation pattern' similar to that of the stars, with the north-west side receding and the south-east side approaching, although it is quite clear that there are other important kinematic components, evidenced by large deviations from simple rotation. Particularly conspicuous is a blueshifted region to the north-east, showing velocity values up to ≈ -100 km s^{-1}, extending by ∼1 arcsec from the nucleus. The Brγ velocity field shows no rotation and the total velocity range is only ≈50 km s^{-1}.

In the right-hand panels of Fig. 7 we present the velocity dispersion (σ) maps obtained from measurements of the FWHM of the emission lines, such that σ = FWHM/2.355. The σ values were corrected for the instrumental broadening and the mean uncertainties are 6 per cent for H_2 and 22 per cent for Brγ. The H_2 σ map has values in the range ∼40–100 km s^{-1}. A partial ring of low velocity dispersion values ($\sigma \approx 45$ km s^{-1}) is observed surrounding the nucleus, while higher values ($80 \leqslant \sigma \leqslant 100$ km s^{-1}) are observed over most of the remaining field. The Brγ σ map presents the highest values of up to ≈100 km s^{-1} at the nucleus – but there are uncertainties in these σ values due to the broad component contribution – and at ≈0.8 arcsec to the south-west, close to the western tip of the 3.6-cm radio structure. At positions away from the nucleus the Brγ σ is lower than 40 km s^{-1}.

5.1 Gas 'tomography'

The high spectral resolution of the data has allowed us to slice the emission-line profiles of H_2 λ2.1218 μm and [Ca VIII] λ2.3211 μm into a sequence of velocity bins. With this 'tomography' technique, we can sample the kinematics along the whole emission-line profile, including the wings. In order to obtain the 'tomography' images, we resampled the spectra into bins of 1 Å with the scombine IRAF task and then combined the two sets of observations into a single data cube using the tasks scombine and imcombine. The velocity slices were obtained after subtraction of the continuum determined as averages of the fluxes from both sides of the emission line. The slices correspond to velocity bins of ≈42 km s^{-1} (3 Å) and are shown in Figs 8 and 9. In these figures, each panel presents flux levels in logarithmic units for the velocity slice shown. The zero velocity is adopted as the systemic velocity of the stars obtained from the stellar kinematic modelling.

The slices trace the gas from negative (blueshifts) to positive (redshifts) velocities relative to the systemic velocity of the stars. For H_2, the highest blueshifts, which reach ≈−190 km s^{-1}, are observed predominantly to the north-east along a curved elongated structure

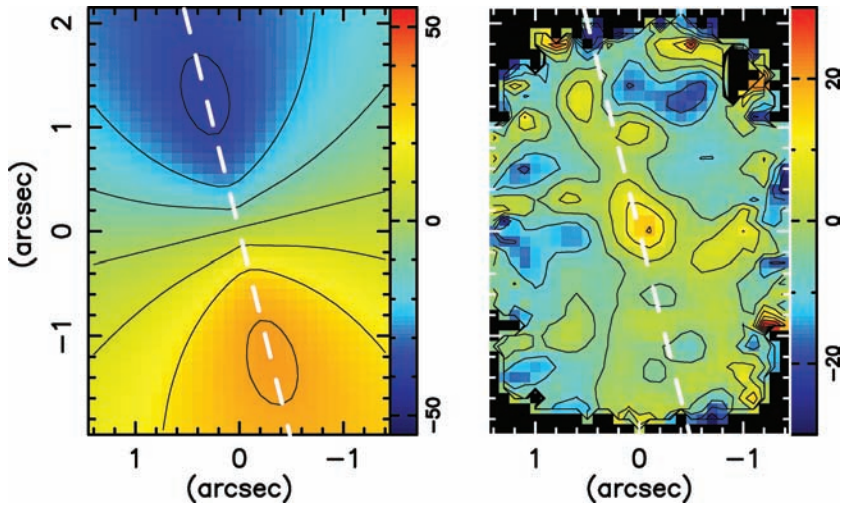

Figure 5. Rotating disc model for the stellar kinematics of NGC 4051 (left-hand panel) and residual map – observed velocity field less model (right-hand panel). The dashed lines mark the positions of the line of nodes.

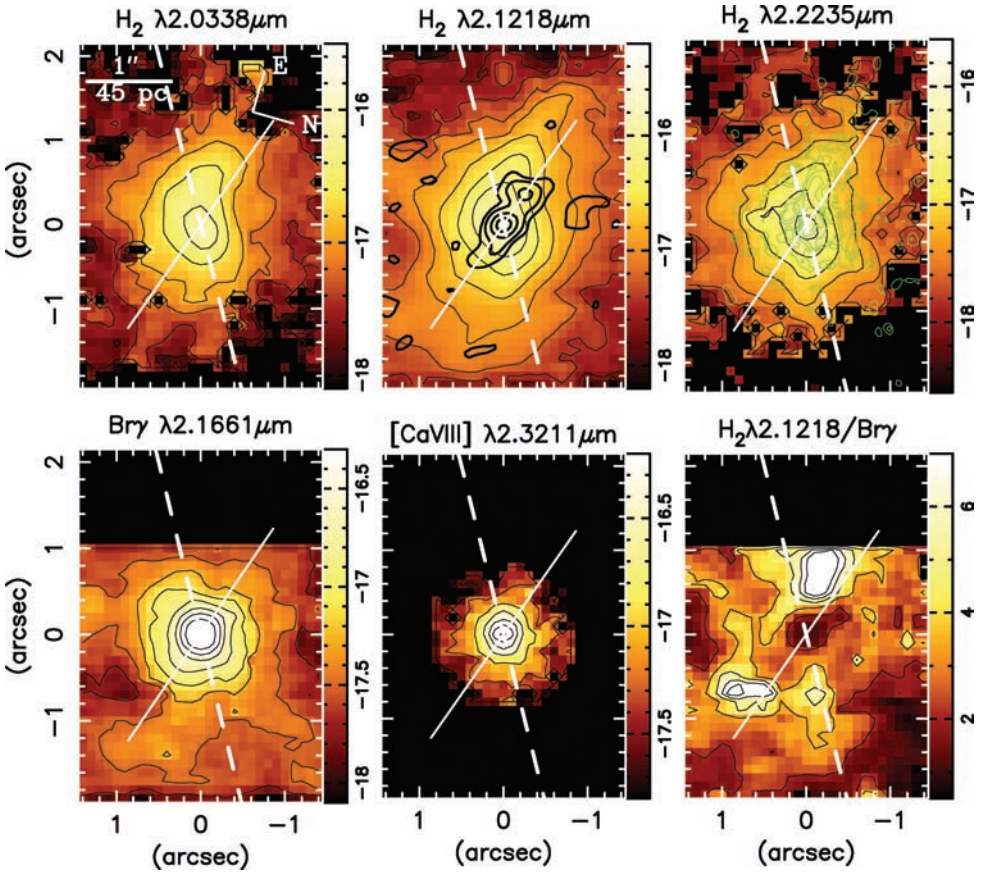

Figure 6. Top: from left- to right-hand side: H_2 $\lambda = 2.0335$, 2.1218 and 2.2235 μm flux maps; bottom left-hand panel: Brγ flux distributions; bottom middle panel: [Ca VIII]λ2.3211 μm flux distributions and bottom right-hand panel: H_2 λ2.1218/Brγ line ratio. The thick black contours overlaid to the H_2 λ2.1218 μm intensity map are from the VLA radio 3.6 cm continuum image, thin black lines are isointensity contours for each panel and the green contours are from an [O III] narrow-band image from *HST*. The spatial scale and orientation shown at the top left-hand panel are the same for all panels. The dashed white line represent the line of nodes of the stellar velocity field and the full white line represent the PA which connects the two radio emission peaks.

similar to the one observed in the radial velocity map (top left-hand panel of Fig. 7). This structure – whose morphology in Fig. 8 can be described as a curved arm – dominates the emission from ≈ -190 to $\approx -60\,\mathrm{km\,s^{-1}}$. At velocities close to systemic, the emission is approximately symmetric and dominated by a region of $\approx$1 arcsec radius centred at the nucleus. As the slices reach positive velocities, the dominant structure is another curved arm extending to $\approx$2 arcsec to the west of the nucleus. The highest redshifts reach $\approx 160\,\mathrm{km\,s^{-1}}$.

For [Ca VIII], we show in Fig. 9 the highest velocity bins and exclude a few low velocity bins where the kinematics are similar. The highest blueshifts reach $\approx -250\,\mathrm{km\,s^{-1}}$, which are higher than those observed for the H_2 emitting gas, while the highest redshifts reach velocities of $170\,\mathrm{km\,s^{-1}}$ similar to the ones observed for H_2.

We opted not to show slices in the Brγ emission-line profile due to the fact that its narrow component is indeed narrow and quite symmetric, and close to the nucleus it is hard to deblend it from the broad-line profile, which introduces too much uncertainty in the derived kinematics.

6 DISCUSSION

6.1 Stellar kinematics

As observed in the top left-hand panel of Fig. 3 and in Fig. 4 the turnover of the rotation curve occurs at only $\approx$55 pc from the nucleus, suggesting that the stellar motions are dominated by a highly concentrated gravitational potential. This is also supported by the small value obtained for the scalelength ($A = 39.7$ pc) from the modelling of the velocity field. The derived parameters are in approximate agreement with the ones derived by Barbosa et al. (2006) from a similar modelling using optical IFU data for a field of view of $\approx 7 \times 5$ arcsec^2 ($315 \times 225\,\mathrm{pc}^2$). The exception is our value of $\Psi_0 = 120^\circ$, which is $\sim 13^\circ$ larger than theirs. On the other hand, our Ψ_0 is $\sim 13^\circ$ smaller than the one derived by Dumas et al. (2007) from stellar kinematics obtained over the much larger field of view of $\approx 50 \times 40$ arcsec^2 ($2250 \times 1800\,\mathrm{pc}^2$). We attribute these differences to the differences in field of view, considering also that our field of view, which corresponds to $130 \times 180\,\mathrm{pc}^2$ at the galaxy, is only sampling the stellar kinematics very close to the nucleus.

For an orientation of the line of nodes of $\Psi_0 = 120^\circ$, and assuming that the spiral arms of NGC 4051 are trailing (orientation of the arms is shown in Fig. 1), we conclude that the north-east is the far side and the south-west is the near side of the galaxy.

The stellar velocity dispersion values show patches with lower values ($\approx$40–50 km s^{-1}) on top of a common background of values ranging from 60 to 70 km s^{-1}. A possible interpretation is that these patches are colder regions with more recent star formation than the underlying bulge. This is supported by optical spectra of the nuclear region which show clear signatures of intermediate age stars (Cid Fernandes et al. 2003). A very small σ drop is observed right at the

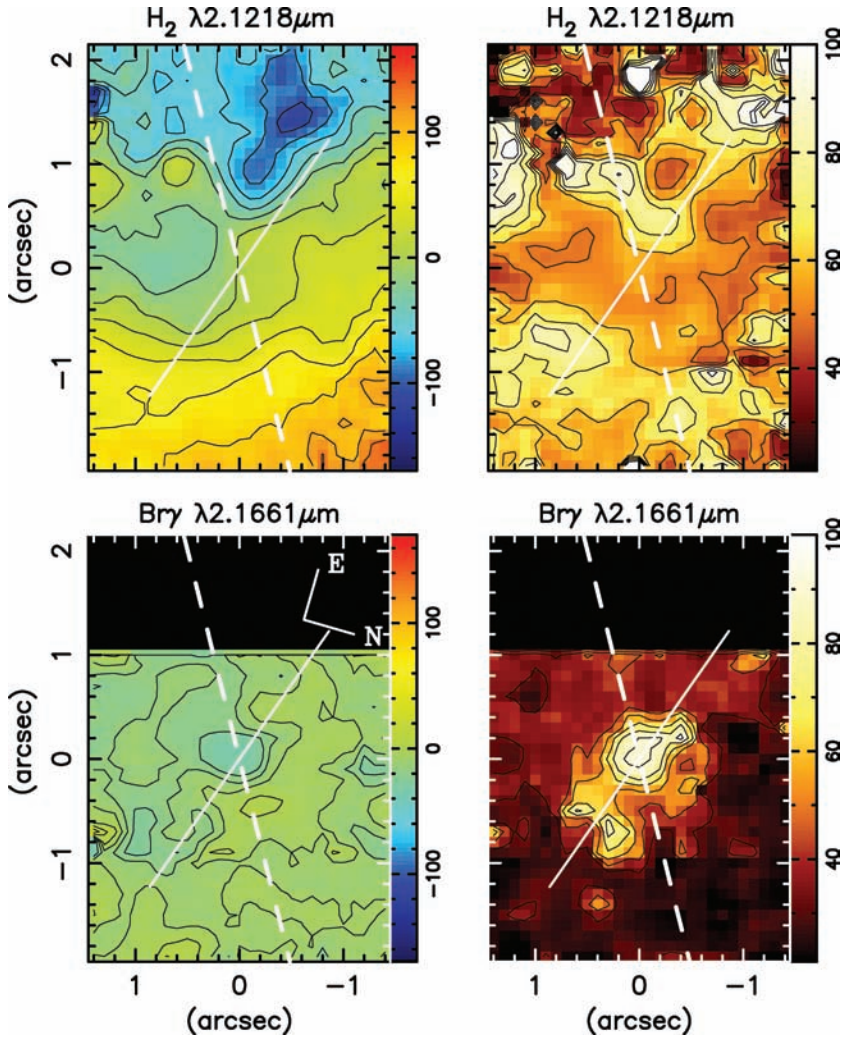

Figure 7. Left-hand panels: velocity field for the H_2 λ2.1218 μm (top) and Brγ (bottom) emission lines. Right-hand panels: velocity dispersion maps for the same emission lines. The contours and lines are as described in Fig. 6, as well as the spatial scale.

nucleus, but we take this result with caution because of the obvious contamination of the spectra of the nuclear region by emission from dust and broad emission lines.

We can estimate the mass of the SMBH ($M_{\rm BH}$) from the bulge stellar velocity dispersion (σ_*) as $\log(M_{\rm BH}/{\rm M}_\odot) = \alpha + \beta \log(\sigma_*/\sigma_0)$, where $\alpha = 8.13 \pm 0.06, \beta = 4.02 \pm 0.32$ and $\sigma_0 = 200\,{\rm km\,s^{-1}}$ (Tremaine et al. 2002). Adopting $\sigma_* \approx 60\,{\rm km\,s^{-1}}$ as representative of the bulge (top right-hand panel of Fig. 3), we obtain $M_{\rm BH} = 1.1 \pm 0.3 \times 10^6\,{\rm M}_\odot$. This value is in good agreement with those obtained by previous authors from reverberation mapping and scaling relations (Kaspi et al. 2000; Shemmer et al. 2003). For this mass, the radius of influence of the SMBH is ≈1.3 pc, thus not resolved at the spatial resolution of our data.

6.2 Gas kinematics

The simultaneous observation of the stellar and gaseous kinematics allowed us to construct residual maps for the gaseous kinematics relative to the stellar kinematics model described in Section 3.4. The residual map for the H_2 emitting gas is presented in Fig. 10. The most conspicuous feature in this map is the elongated structure to the north-east, which shows blueshifts of up to $\approx -100\,{\rm km\,s^{-1}}$, also seen in the corresponding velocity slices in Fig. 8. These blueshifts could be either due to an inflow, if the gas is located in the plane, as the north-east is the far side of the galaxy; or to an outflow, if the gas is extended to high latitudes (above the plane), e.g. in a conical structure oriented towards us. We discuss below these two possibilities.

The outflow interpretation is supported by the following facts. (1) The elongated north-east structure is *approximately* oriented along the radio jet. (2) A *similar* structure and blueshifts have been observed by Barbosa et al. (in preparation) in IFU observations of [S III] λ9069 emitting gas, who found, in addition, redshifts to the south-west, which appear to be due to a counterpart conical outflow related to the south-west part of the radio jet, probably located behind the galactic plane and being directed away from us. (3) The velocity dispersion and line ratio maps show increased values in regions close to the tips of the radio jet.

The inflow interpretation is, on the other hand, supported by the following facts. (1) The orientation of the north-east blueshifted region is not well aligned with the direction of the radio jet, but is shifted by ∼0.5 arcsec to the south–south-east (see Fig. 8). (2) The blueshifted region is elongated and curved as if it belonged to a spiral arm ending at the nucleus, while the blueshifted structure observed

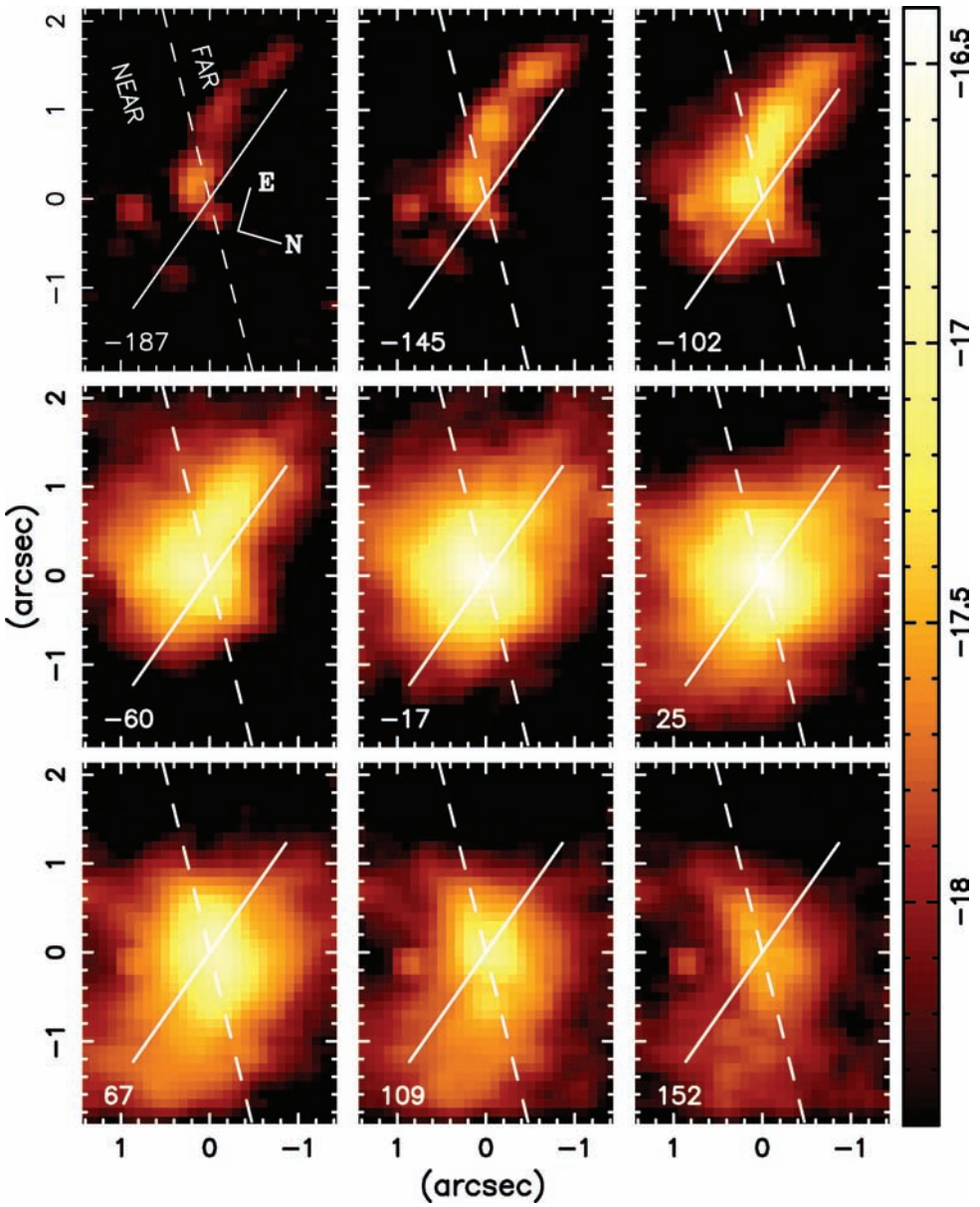

Figure 8. Velocity slices along the H_2 profile with a velocity bin of $\approx$42 km s^{-1}. The cross marks the position of the nucleus and the intensity scale is logarithmic. The zero velocity is the systemic velocity obtained from the stellar kinematics modelling. The near and far side of the galaxy are indicated in the top left-hand panel (under the assumption that the spiral arms are trailing).

in the [S III] λ9069 emitting gas by Barbosa et al. (in preparation) shows a more conical shape whose axis is better aligned with the direction of the radio jet. (3) There is no redshifted counterpart in H_2 as observed for the [S III] emitting gas. There is instead a redshifted structure observed in the velocity slices (see Fig. 8) also curved as belonging to a spiral arm in the near side (south-west) of the galaxy.

Considering the arguments above we favour the inflow interpretation. The blueshifts to the north-east and redshifts to the south-west observed in the H_2 emitting gas would then be due to inflow of molecular gas in the galaxy plane along nuclear spiral arms. The presence of such arms is supported by the structure map of the nuclear region of NGC 4051 presented by Simões Lopes et al. (2007), which shows similar spiral structure with the same curvature and orientation of the arms in an *HST* optical image of the nuclear region of NGC 4051. The structure map also shows a lot of obscuration against the near side of the galaxy, which would explain why the flux of the redshifted gas emission is fainter than that of the blueshifted gas on the far side of the galaxy. The enhancements in the gas velocity dispersions and increase in line emission ratios observed in H_2 and Brγ emitting gas can be understood if the radio jet is launched at a relatively small angle to the galaxy plane compressing the circumnuclear ISM close to the nucleus.

In a recent study aimed at investigating the interaction between the radio jet and line emission in the NLR of the Seyfert galaxy ESO 428−G14 using GNIRS IFU data we found a close association of the [Fe II] and H I emission-line distributions and kinematics with the radio emission distribution (Riffel et al. 2006b), a result also found in some studies (e.g. Falcke, Wilson & Simpson 1998; Bicknell et al. 2000; Tilak et al. 2005; Barbosa et al., in preparation), but also contested by others (e.g. Kaiser et al. 2000; Das et al. 2005).

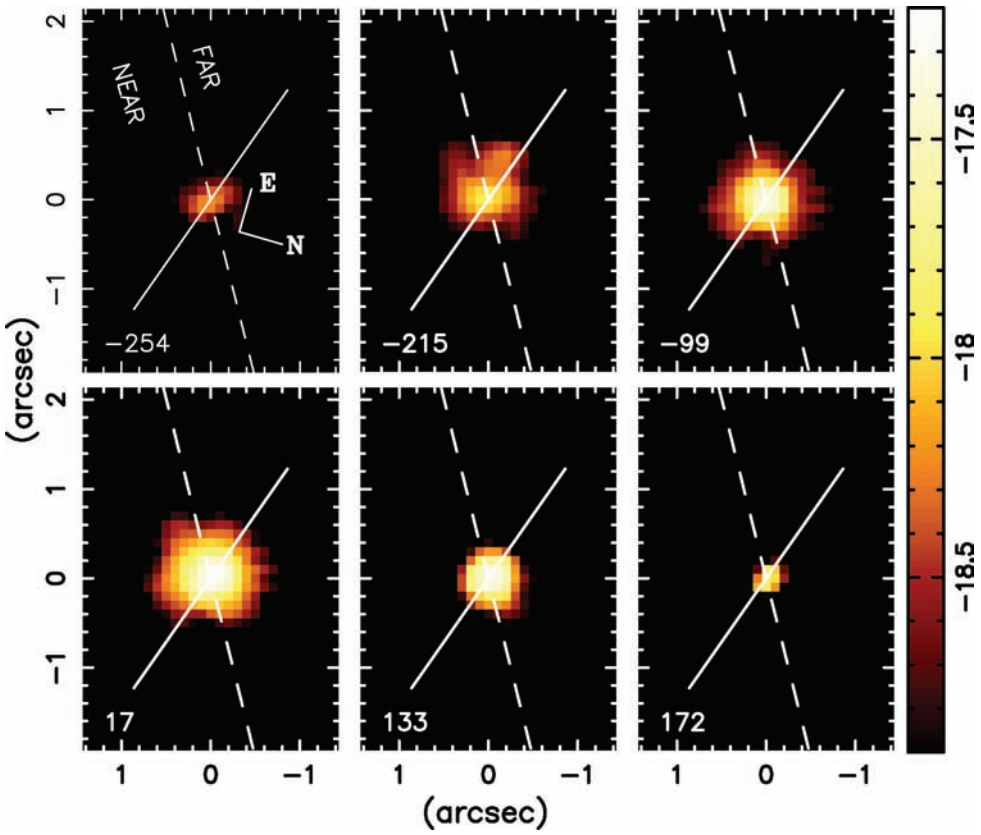

Figure 9. Same as Fig. 8 for the [Ca VIII] emission-line profile.

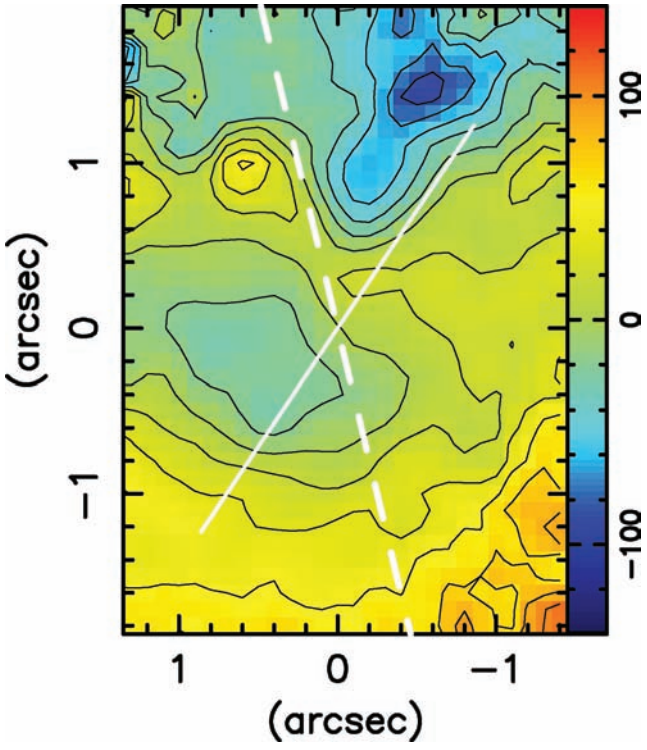

Figure 10. Difference between the H_2 and stellar kinematics. The white dashed line shows the orientation of the line of nodes and the full white line shows the PA of the radio emission.

In ESO 428−G14, Riffel et al. (2006b) concluded that the H_2 kinematics was distinct from that in the other emission lines: although part of the H_2 emitting gas was affected by interaction with the radio jet, most of it was located in the galaxy plane and was not affected by the radio jet. A less disturbed kinematics for H_2 than for other emission lines was also found in a near-IR study of the gas emission around the nuclei of the Seyfert galaxies NGC 2110 and Circicus (Storchi-Bergmann et al. 1999). These studies thus also support our favoured interpretation in the present study: most of the H_2 emission is located in the plane and is not related to the outflow. It is instead, flowing towards the nucleus along spiral arms.

The Brγ emitting gas is almost all at the systemic velocity as observed in the bottom left-hand panel of Fig. 7 and seems to show no rotation, which leads us to conclude that most of the Brγ emitting gas is not restricted to the plane of the galaxy.

6.3 [Ca VIII] coronal emission

Coronal lines are forbidden transitions from highly ionized species which extend from the unresolved nucleus up to distances between a few tens to a few hundreds of parsecs, and usually present blue wings and are broader than low ionization lines (e.g. Rodríguez-Ardila et al. 2006, and references therein). Thus, it is possible to resolve the coronal line region for the closest active galaxies. In NGC 4051, the [Ca VIII] coronal emission line at 2.3211 μm is indeed resolved, presenting extended emission in a circular region around the nucleus with diameter of ≈75 pc. Blueshifts of up to $-250\,\mathrm{km\,s^{-1}}$ are observed very close to the nucleus (within the inner ≈25 pc), a value that is much higher than that observed for Brγ and H_2 emission lines. The mean velocity dispersion is $150\,\mathrm{km\,s^{-1}}$,

which is about two to three times higher than that obtained the other lines as well. This kinematics together with the compact flux distribution supports the interpretation that the coronal lines are produced close to the nucleus, and probably in the transition region between the broad-line region (BLR) and the NLR as suggested by previous authors. The spatial extent of the emission, the blueshifts and the σ values observed in NGC 4051 are similar to the ones obtained for the Seyfert 2 galaxy Circinus, while for more active galaxies such values tend to be higher (Rodríguez-Ardila et al. 2006).

6.4 Mass of the emitting gas

The mass of hot H_2 can be estimated as (e.g. Scoville et al. 1982)

$$M_{H_2} = \frac{2m_p\, F_{H_2\lambda 2.1218}\, 4\pi d^2}{f_{v=1,J=3} A_{S(1)}\, h\nu} = 5.0776 \times 10^{13} \left(\frac{F_{H_2\lambda 2.1218}}{\mathrm{erg\,s^{-1}\,cm^{-2}}}\right) \left(\frac{d}{\mathrm{Mpc}}\right)^2, \quad (3)$$

where m_p is the proton mass, $F_{H_2\lambda 2.1218}$ is the line flux, d is the galaxy distance and M_{H_2} is given in solar masses. As proposed by Scoville et al. (1982), we assume a typical vibrational temperature of $T_{vib} = 2000$ K, which implies a population fraction $f_{v=1,J=3} = 1.22 \times 10^{-2}$ and a transition probability $A_{S(1)} = 3.47 \times 10^{-7}\,s^{-1}$ (Turner, Kirby-Docken & Dalgarno 1977). The line flux should be corrected for the intrinsic $E(B-V)$, but for NGC 4051, $E(B-V)$ is small (Riffel et al. 2006a) and thus we do not apply any correction. For the east–north-east inflow region we obtain $F_{H_2\lambda 2.1218} = 2.1 \times 10^{-15}$erg s^{-1}cm^{-2} integrated within the approximately triangular region which includes blueshifts larger than $-100\,km\,s^{-1}$ in Fig. 10 and obtain a mass of $M_{H_2} \approx 9.3\,M_\odot$. Integrating now the $H_2\,\lambda 2.1218\,\mu m$ emission over the same field where the Brγ is observed (the central $130 \times 135\,pc^2$) we obtain $F_{H_2\lambda 2.1218} = 1.5 \times 10^{-14}\,erg\,s^{-1}\,cm^{-2}$ and thus $M_{H_2} \approx 66\,M_\odot$.

The above masses are small, but we point out that in the nuclear region of galaxies it has been shown that the hot-to-cold mass ratio ranges between 10^{-7} and 10^{-5} (Dale et al. 2005), suggesting that the total mass of molecular gas can be orders of magnitude larger than the value measured directly from the H_2 emission.

The mass of the ionized hydrogen can be estimated as $M_{H\,II} = m_p N_e V_{H\,II}$, where N_e is the electron density and $V_{H\,II}$ is the volume of the emitting region. Replacing $N_e V_{H\,II}$ by the expression given in Scoville et al. (1982) we obtain

$$M_{H\,II} = 2.88 \times 10^{17} \left(\frac{F_{Br\gamma}}{\mathrm{erg\,s^{-1}cm^{-2}}}\right) \left(\frac{d}{\mathrm{Mpc}}\right)^2, \quad (4)$$

where $M_{H\,II}$ is given is solar masses, and we assume an electron temperature $T = 10^4$ K and electron density $N_e = 100\,cm^{-3}$. The total integrated Brγ flux is $F_{Br\gamma} \approx 5.8 \times 10^{-15}\,erg\,s^{-1}\,cm^{-2}$ and thus $M_{H\,II} \approx 1.4 \times 10^5\,M_\odot$. The mass of ionized gas is thus about 2000 larger than the mass of hot H_2 gas.

Using the above calculated mass M_{H_2} for the east–north-east blueshifted region we can estimate the flux of inflowing hot molecular gas under the assumption that this gas is streaming towards the nucleus. We calculate the hot H_2 mass crossing a circular cross-section by $\dot{M}_{H_2} = 2m_p N_{H_2} v\, \pi r^2$, where v is the inflowing velocity and r is the radius of the circular cross-section. The maximum blueshift velocities occur at 1.2 arcsec east–north-east of the nucleus where the cross-section radius of the structure shown in Fig. 10 is estimated to be $r = 0.55$ arcsec ≈ 25 pc. Assuming $v = 100\,km\,s^{-1}$ and conical geometry to calculate the H_2 density, we obtain $\dot{M}_{H_2} = 2.5 \times 10^{21}\,g\,s^{-1} \approx 4 \times 10^{-5}\,M_\odot\,yr^{-1}$. This rate is probably up to two times larger if we consider a similar inflow along the west–south-west spiral arm, observed in redshift.

The mass accretion rate necessary to power the active nucleus can be estimated by $\dot{M} = L_{bol}/(c^2\eta)$, where L_{bol} is the bolometric luminosity, c is the light speed and η is the efficiency of conversion of the rest-mass energy of the accreted material into radiation. Assuming a typical value of $\eta \approx 0.1$ and using $L_{bol} = 2.7 \times 10^{43}\,erg\,s^{-1}$ from Ogle et al. (2004) we obtain $\dot{M} = 4.7 \times 10^{-3}\,M_\odot\,yr^{-1}$. The H_2 mass inflow rate calculated above is then about 100 times smaller than the accretion rate needed to power the AGN of NGC 4051, supporting additional contribution of cold non-emitting gas to the mass inflow rate.

6.5 H_2 excitation

The H_2 lines can be excited by three distinct processes: fluorescent excitation through absorption of soft-UV photons (912–1108 Å) in the Lyman and Werner bands (Black & van Dishoeck 1987), excitation by X-ray heating (Maloney, Hollenbach & Tielens 1996) and excitation by shocks (Hollembach & McKee 1989). The first is usually considered a non-thermal process while the other two are considered thermal processes. Several studies investigated the H_2 excitation mechanisms (e.g. Draine & Woods 1990; Veilleux, Goodrich & Wilson 1997; Quillen et al. 1999; Bellamy & Tadhunter 2004; Rodríguez-Ardila, Riffel & Pastoriza 2005; Riffel et al. 2006b; Riffel, Rodríguez-Ardila & Pastoriza 2006a; Zuther et al. 2007).

Quillen et al. (1999) have looked for correlations of the H_2 emission with radio 6 cm and hard X-ray fluxes. They found no correlation with X-rays, suggesting X-rays heating is not the dominant H_2 excitation mechanism, and found a weak correlation with radio 6 cm, suggesting that no single mechanism is likely to be responsible for the molecular hydrogen excitation in Seyfert galaxies. Draine & Woods (1990) propose that most of the H_2 line emission originates in molecular gas which is heated by transient X-ray irradiation. Hard X-rays from the AGN also have been proposed by Wilman et. al. (2000) and Bellamy & Tadhunter (2004) as the dominant excitation mechanism of H_2 emission in Cygnus A. Zuther et al. (2007) using the Maloney et al. (1996) X-rays excitation models found that the X-ray emission can account for some H_2 excitation for the starburst/Seyfert galaxy Mrk 609. For the case of ESO 428−G14 we concluded that shocks produced by a radio jet play a fundamental role in the kinematics and excitation of the $H_2\lambda 2.1218$ emission line in regions cospatial with the radio emission and X-rays are important in regions away from the radio structures (Riffel et al. 2006b).

The $H_2\,\lambda 2.2477/\lambda 2.1218$ line ratio is commonly used to distinguish between thermal (∼0.1–0.2) and fluorescent (∼0.55) excitation mechanisms for the H_2 emitting gas (Mouri 1994; Reunanen, Kotilainen & Prieto 2002; Rodríguez-Ardila et al. 2005), while the $H_2\,\lambda 2.0338/\lambda 2.2235$ ratio is used to determine the thermal excitation temperature. The $H_2\,\lambda 2.2477\,\mu m$ emission line is only marginally detected in our individual spectra, so we integrated the flux of this line over the whole IFU field obtaining $H_2\,\lambda 2.2477/\lambda 2.1218 \approx 0.12 \pm 0.02$, indicating that the emitted H_2 is excited by thermal processes.

The rotational and vibrational temperatures for the molecular gas can also be used to distinguish between thermal and fluorescent excitation: for thermal excitation the vibrational and rotational temperatures must be similar and for fluorescent excitation the vibrational temperature must be higher than the rotational temperature – non-local UV photons overpopulate the highest energy levels compared to the population distribution expected for a Maxwell–Boltzmann distribution. The rotational temperature can be obtained

by $T_{\rm rot} \cong -1113/\ln(0.323 \times F_{\rm H_2\lambda2.0338}/F_{\rm H_2\lambda2.2235})$ and the vibrational temperature by $T_{\rm vib} \cong 5600/\ln(1.355 \times F_{\rm H_2\lambda2.1218}/F_{\rm H_2\lambda2.2477})$ (Reunanen et al. 2002). For NGC 4051 we obtain $H_2\,\lambda2.0338/\lambda2.2235 = 1.8 \pm 0.28$ and $H_2\,\lambda2.1218/\lambda2.2477 = 8.4 \pm 1.02$, thus $T_{\rm rot} = 2052^{+746}_{-488}$ K and $T_{\rm vib} = 2305^{+157}_{-120}$ K. The similarity of these two values reinforces thermal processes as the dominant excitation mechanism of the molecular hydrogen. The value obtained for the vibrational temperature supports the assumption ($T_{\rm vib} = 2000$ K) used in equation (3) to obtain the hot H_2 mass.

In order to test if X-ray emission can account for the excitation of the $H_2\,\lambda2.1218$ μm emission line for NGC 4051 we have used the models of Maloney et al. (1996) to estimate the emergent H_2 flux of a gas cloud illuminated by a source of hard X-rays with an intrinsic luminosity $L_{\rm X}$. The cooling is given by the effective ionization parameter $\xi_{\rm eff}$ (Zuther et al. 2007):

$$\xi_{\rm eff} = 1.26 \times 10^{-4} \frac{f_{\rm X}}{n_5 N_{22}^{0.9}}, \quad (5)$$

where $f_{\rm X}$ is the incident hard X-ray flux at the distance d (pc) from the X-ray source, $n_5[10^{-5}\,{\rm cm}^{-3}]$ is the total hydrogen gas density and N_{22} $[10^{22}\,{\rm cm}^2]$ is the attenuating column density. Using $f_{\rm X} = 2.3 \times 10^{-11}\,{\rm erg\,cm^{-2}\,s^{-1}}$ and $N_{\rm H} = 1.32 \times 10^{20}\,{\rm cm}^{-2}$ obtained from the *ASCA* Tartarus data base we can calculate $\xi_{\rm eff}$. Maloney et al. (1996) calculate emergent fluxes for two gas densities, 10^5 and $10^3\,{\rm cm}^{-3}$. We calculate the effective ionization parameter for three different distances of the AGN (25, 50 and 75 pc), and for the same gas densities of Maloney et al. (1996). Using this and their figs 6(a) and (b) we can obtain the emergent intensity of the $H_2\,\lambda2.1218$ μm emission line. In Table 1 we present the calculated effective ionization parameter and the emergent flux for an aperture of 0.1×0.1 arcsec^2 – corresponding to a solid angle 2.34×10^{-13} sr – in erg cm^{-2} s^{-1}. In this table we also present the observed $H_2\,\lambda2.1218$ μm obtained by the average of the H_2 flux in a ring with radius d and width of 0.2 arcsec.

By comparing the emergent fluxes from Table 1 obtained by X-ray heating models with the observed fluxes we conclude that excitation by X-ray heating can account for most of the observed H_2 flux.

Another line ratio commonly used to investigate the H_2 excitation is $H_2\,\lambda2.1218/{\rm Br}\gamma$. In starburst galaxies, where the main heating agent is UV radiation, $H_2/{\rm Br}\gamma < 0.6$ (Rodríguez-Ardila et al. 2005), while for Seyferts this ratio is larger ($0.6 < H_2/{\rm Br}\gamma < 2$) because of additional H_2 emission excited by shocks or by X-rays from the AGN (Rodríguez-Ardila et al. 2005). As observed in the bottom right-hand panel of Fig. 6, NGC 4051 presents $H_2/{\rm Br}\gamma = 1 \pm 0.2$ at the nucleus, which is a typical value for AGNs. The highest values reach $H_2/{\rm Br}\gamma = 8 \pm 1.9$ and are observed east-north-east and to the west–south-west of the nucleus, close to the tips of the radio jet, supporting some contribution of shocks by the radio jet to the excitation of the molecular hydrogen in these regions. On the other hand, the interpretation of this line ratio should be considered with caution due to the fact that the bulk of H_2 emission seems to originate from the disc while the Brγ emission seems not to be restricted to the disc.

Table 1. Comparison of the observed $H_2\,\lambda2.1218$ μm fluxes and calculated using models of Maloney et al. (1996) for an aperture of 0.1×0.1 arcsec^2 for hydrogen densities $n = 10^5$ and $10^3\,{\rm cm}^{-3}$.

	Observed	$n = 10^5\,{\rm cm}^{-3}$		$n = 10^3\,{\rm cm}^{-3}$	
d(pc)	log(F_{H_2})	log($\xi_{\rm eff}$)	log(F_{H_2})	log($\xi_{\rm eff}$)	log(F_{H_2})
25	−16.4	−1.7	−14.7	–	–
50	−17.0	−2.3	−17.2	−0.3	−15.8
75	−17.3	−2.7	−17.0	−0.7	−15.7

7 CONCLUSIONS

We have analysed 2D near-IR $K-$band spectra from the inner ≈150 pc of the NLS1 galaxy NGC 4051 obtained with the Gemini NIFS at a sampling of 4.5×4.5 pc^2 at the galaxy and spectral resolution of ≈3 Å. We have mapped the stellar and gaseous kinematics, and the emission-line flux distributions and ratios of the molecular and ionized hydrogen. The main conclusions of this work are as follows.

(i) The turnover of the stellar rotation curve is at only ≈55 pc from the nucleus, suggesting that the stellar motions are dominated by a highly concentrated gravitational potential, a result confirmed by modelling using a Plummer gravitational potential, as we obtain a small scalelength, A ≈39 pc. This result supports the findings of Barbosa et al. (2006) based of optical data. The mean velocity dispersion of the bulge (∼60 km s^{-1}) implies a SMBH mass of $\sim 10^6\,{\rm M}_\odot$. Within the bulge, we find patches of lower velocity dispersions, which we attribute to recent star formation.

(ii) The gas kinematics is distinct for each emission line: the Brγ emission line shows velocities restricted to within ∼30 km s^{-1} from systemic, without evidence of bulk motions, suggesting that the ionized gas is not restricted to the galactic plane, while much larger blueshifts and redshifts are observed for both the [Ca VIII] and H_2 emitting gas. The Brγ velocity dispersion is small (∼40 km s^{-1}) over most of the field, except around the nucleus at a location close to the south-west tip of the radio jet, suggesting some energy injection in the gas by interaction with the radio jet.

(iii) The [Ca VIII] coronal emission line is compact but resolved, extending over a circular region of radius ≈35 pc around the nucleus. It also present the largest velocity blueshifts (−250 km s^{-1}) and velocity dispersion (150 km s^{-1}) of the emission lines studied here, supporting an origin close to the active nucleus, possibly in the transition region between the BLR and the NLR.

(iv) The H_2 emitting gas seems to be mostly restricted to the galaxy plane. The most conspicuous kinematic features are a curved elongated blueshifted structure to the north-east, interpreted as gas inflow along a nuclear spiral arm in the far side of the galaxy, and a curved, redshifted structure to the south-west, interpreted as gas inflow along a nuclear spiral arm in the near side of the galaxy. Estimates of the mass inflow rate in hot H_2 gives $\dot{M}_{H_2} \approx 4 \times 10^{-5}\,{\rm M}_\odot\,{\rm yr}^{-1}$, which is ∼100 times smaller than the nuclear accretion rate necessary to power the active nucleus of NGC 4051, supporting the presence of additional inflow of cold non-emitting gas. This is not the first time we have been able to map inflows towards an active nucleus along nuclear spiral arms. In two previous studies we (Fathi et al. 2006; Storchi-Bergmann et al. 2007) have mapped streaming motions towards the active nucleus along nuclear spirals in the galaxies NGC 1097 and 6951 although in ionized gas. As nuclear spirals are ubiquitous around AGN (Prieto, Maciejewski & Reunanen 2005; Simões Lopes et al. 2007), such inflows seem to be a 'universal' mechanism to bring gas inwards to feed the SMBH within the inner few hundred parsecs of the galaxy.

(v) The total mass of hot H_2 is estimated to be of the order of $66\,{\rm M}_\odot$, while that of H II is estimated to be $1.4 \times 10^5\,{\rm M}_\odot$.

(vi) From the H_2 line ratios we conclude that H_2 is excited by thermal processes – heating by X-rays from the AGN and shocks produced by the radio jet. We conclude, based on X-ray excitation models of Maloney et al. (1996) that X-ray heating can account

for the observed emission, but the H_2 λ2.1218 μm/Brγ line ratio supports some contribution from shocks in the regions where the radio jet interacts with the H_2 emitting gas.

ACKNOWLEDGMENTS

Based on observations obtained at the Gemini Observatory, which is operated by the Association of Universities for Research in Astronomy, Inc., under a cooperative agreement with the NSF on behalf of the Gemini partnership: the National Science Foundation (United States), the Science and Technology Facilities Council (United Kingdom), the National Research Council (Canada), CONICYT (Chile), the Australian Research Council (Australia), CNPq (Brazil) and SECYT (Argentina). Basic research in astronomy at the NRL is supported by NRL 6.1 Base funding. The National Radio Astronomy Observatory is a facility of the National Science Foundation operated under cooperative agreement by Associated Universities, Inc. This research has made use of the NED which is operated by the Jet Propulsion Laboratory, California Institute of Technology, under contract with the National Aeronautics and Space Administration. This research has made use of the Tartarus data base, created by Paul O'Neill and Kirpal Nandra at Imperial College London and Jane Turner at NASA/GSFC. Tartarus is supported by funding from PPARC, and NASA grants NAG5-7385 and NAG5-7067. This work has been partially supported by the Brazillian institution CNPq.

REFERENCES

Adler D. S., Westpfahl D. J., 1996, AJ, 111, 735
Barbosa F. K. B., Storchi-Bergmann T., Cid Fernandes R., Winge C., Schmitt H., 2006, MNRAS, 371, 170
Bellamy M. J., Tadhunter C. N., 2004, MNRAS, 353, 105
Bicknell G. V., Sutherland R. S., van Breugel W. J. M., Dopita M. A., Dey A., Miley G. K., 2000, ApJ, 540, 678
Black J. H., van Dishoeck E. F., 1987, ApJ, 322, 412
Blandford R. D., McKee C. F., 1982, ApJ, 255, 419
Boisson C., Joly M., Moultaka J., Pelat D., Serote Roos M., 2000, A&A, 357, 850
Boone F. et al., 2007, A&A, 471, 113
Cappellari M., Emsellem E., 2004, PASP, 116, 138
Christopoulou P. E., Holloway A. J., Sreffen W., Miundell C. G., 1997, MNRAS, 284, 385
Cid Fernandes R., Heckman T., Schmitt H., González Delgado R. M., Storchi-Bergmann T., 2001, ApJ, 558, 81
Cid Fernandes R., Schmitt H., González Delgado R. M., Storchi-Bergmann T., Heckman T., Rodrigues Lacerda R., 2003, in Perez E., Gonzalez Delgado R. M., Tenorio-Tagle G., eds, ASP Conf. Ser. Vol. 297, Star Formation Through Time. Astron. Soc. Pac., San Francisco, p. 357
Cid Fernandes R., González Delgado R. M., Storchi-Bergmann T., Martins L. P., Schmitt H., 2005, MNRAS, 356, 270
Crenshaw D. M., Kraemer S. B., 2000, ApJ, 532, L101
Dale D. A., Sheth K., Helou G., Regan M. W., Hüttemeister S., 2005, ApJ, 129, 2197
Das V. et al., 2005, AJ, 130, 945
Davies R. I. et al., 2006, AJ, 646, 754
Draine B. T., Woods D. T., 1990, ApJ, 363, 464
Dumas G., Mundell C. G., Emsellem E., Nagar N. M., 2007, MNRAS, 379, 1249
Emsellem E. et al., 2004, MNRAS, 352, 721
Falcke H., Wilson A. S., Simpson C., 1998, ApJ, 502, 199
Fathi K., Storchi-Bergmann T., Riffel R. A., Winge C., Axon D. J., Robinson A., Capetti A., Marconi A., 2006, ApJ, 641, L25
Ferrarese L., Merritt D., 2000, ApJ, 539, L9
García-Burillo S. et al., 2003, A&A, 407, 485
Gebhardt K. et al., 2000, ApJ, 539, L13
Hollembach D., McKee C. F., 1989, ApJ, 342, 306
Kaiser M. E. et al., 2000, ApJ, 528, 260
Kaneko N., Aoki K., Kosugi G., Ohtani H., Yoshida M., Toyama K., Satoh T., Sasaki M., 1997, AJ, 114, 94
Kaspi S., Smith P., Netzer H., Maoz D., Jannuzi B. T., Giveon U., 2000, ApJ, 533, 631
Knapen J. H., de Jong R. S., Stedman S., Bramich D. M., 2003, MNRAS, 344, 527
Krips M. et al., 2005, A&A, 442, 479
Lawrence A., Watson M. G., Pounds K. A., Elvis M., 1985, MNRAS, 217, 685
Maloney P. R., Hollembach D. J., Tielens A. G. G. M., 1996, ApJ, 360, 55
McGregor P. J. et al., 2003, in Iye M., Moorwood A. F. M., eds, Proc. SPIE Vol. 4841, Instrument Design and Performance for Optical/Infrared Ground-based Telescopes. SPIE, Bellingham, p. 1581
Mouri H., 1994, ApJ, 427, 777
Mundell C. G., Shone D. L., 1999, MNRAS, 304, 475
Nagao T., Taniguchi Y., Murayama T., 2000, AJ, 119, 2605
Ogle P. M., Mason K. O., Page M. J., Salvi N. J., Cordova F. A., McHardy I. M., Priedhorsky W. C., 2004, ApJ, 606, 151
Ponti G., Miniutti G., Cappi M., Maraschi L., Fabian A. C., Sawa K., 2006, MNRAS, 368, 903
Prieto M. A., Maciejewski W., Reunanen J., 2005, ApJ, 130, 1472
Quillen A. C., Alonso-Herrero A., Rieke M. J., Rieke G. H., Ruiz M., Kulkarni V., 1999, ApJ, 527, 696
Reunanen J., Kotilainen J. K., Prieto M., A., 2002, MNRAS, 331, 154
Riffel R. A., Sorchi-Bergmann T., Winge C., Barbosa F. K. B., 2006a, MNRAS, 373, 2
Riffel R., Rodríguez-Ardila A., Pastoriza M. G., 2006b, A&A, 457, 61
Rodríguez-Ardila A., Riffel R., Pastoriza M. G., 2005, MNRAS, 364, 1041
Rodríguez-Ardila A., Prieto M. A., Viegas S., Gruenwald R., 2006, ApJ, 653, 1098
Salvati M. et al., 1993, A&A, 274, 174
Schmitt H. R., Kinney A. L., 1996, ApJ, 463, 498
Schmitt H. R., Storchi-Bergmann T., Cid Fernandes R., 1999, MNRAS, 303, 173
Scoville N. Z., Hall D. N. B., Kleinmann S. G., Ridgway S. T., 1982, ApJ, 253, 136
Shemmer O., Uttley P., Netzer H., McHardy I. M., 2003, MNRAS, 283, 777
Silge J., Gebhardt K., 2003, AJ, 125, 2809
Simões Lopes R. D., Storchi-Bergmann T., de Fátima Saraiva M., Martini P., 2007, ApJ, 655, 718
Storchi-Bergmann T., Winge C., Ward M. J., Wilson A. S., 1999, MNRAS, 304, 35
Storchi-Bergmann T., Raimann D., Bica E. L. D., Fraquelli H. A., 2000, ApJ, 544, 747
Storchi-Bergmann T., Nemmen R. S., Spinelli P. F., Eracleous M., Wilson A. S., Filippenko A. V., Livio M., 2005, ApJ, 624, L13
Storchi-Bergmann T., Dors O. Jr, Riffel R. A., Fathi K., Axon D. J., Robinson A., 2007, ApJ, 660, 959
Tilak A., O'Dea C. P., Tadhunter C., Wills K., Morganti R., Baum S., A., Koekemoer A. M., Dallacasa D., 2005, AJ, 130, 2513
Tremaine S. et al., 2002, ApJ, 574, 740
Turner J., Kirby-Docken K., Dalgarno A., 1977, ApJS, 35, 281
Ulvestad J. S., Wilson A. S., 1984, ApJ, 285, 439
van der Marel R. P., Franx M., 1993, ApJ, 407, 525
Veilleux S. A., 1991, ApJ, 369, 331
Veilleux S. A., Goodrich R. W., Hill G. J., 1997, ApJ, 477, 631
Wilman R. J., Edge A. C., Johnstone R. M., Crawford C. S., Fabian A. C., 2000, MNRAS, 318, 1232
Winge C., Riffel R. A., Storchi-Bergmann T., 2007, http://www.gemini.edu/sciops/instruments/nir/spectemp/index.html
Zuther J., Iserlohe C., Pott J. U., Bertram T., Fischer S., Voges W., Hasinger G., Eckart A., 2007, A&A, 466, 451

This paper has been typeset from a TEX/LATEX file prepared by the author.